Materials Today Bio 29 (2024) 101328

Contents lists available at ScienceDirect

Materials Today Bio

journal homepage: www.journals.elsevier.com/materials-today-bio

Switchable ROS generator and scavenger to prevent the cisplatin induced acute kidney injury and improve efficacy via synergistic chemodynamic/immune therapy

Yanan Ren [a,1], Fei Wu [a,1], Linlin Huo [b,1], Xiao Wang [a], Yong Zhang [a], Mengke Fan [b], Mingya Tan [b], Jiayi Zhao [b], Jingliang Cheng [a,**], Zhenghuan Zhao [b,*], Jianfeng Bao [a,***]

[a] Functional Magnetic Resonance and Molecular Imaging Key Laboratory of Henan Province, Department of Magnetic Resonance Imaging, First Affiliated Hospital of Zhengzhou University, Zhengzhou University, Zhengzhou, 450001, China
[b] College of Basic Medical Sciences, Chongqing Medical University, Chongqing, 400016, China

ARTICLE INFO

Keywords:
Switchable ROS scavenger/generator
Cisplatin adjuvant
Acute kidney injury
Improved therapeutic efficacy

ABSTRACT

Acute kidney injury (AKI) induced by cisplatin (DDP), which is accompanied with the generation of reactive oxygen species (ROS), is a severe side effect during treatment and restricts the application of DDP. In this study, we develop ultrasmall Mn_3O_4 nanozyme (UMON) with tumor microenvironment (TME) responsive ROS scavenging and generating as adjuvant to alleviate DDP induced AKI with improved efficacy. In kidney, UMON with superoxide dismutase and catalase activity acts as ROS scavenger to eliminate ROS generated by DDP, successfully protecting the renal cells/tissue and alleviating AKI during DDP treatment. Alternatively, UMON rapidly responses to the high GSH level in TME and release Mn^{2+} in tumor. This unique feature endows it to generate hydroxyl radicals (•OH) through a Fenton-like reaction and deplete GSH in tumor cell and tissue, achieving high efficient chemodynamic therapy (CDT). More importantly, the Mn^{2+} successfully activates the cGAS-STING pathway, initiating the immune response and effectively inhibiting the tumor metastases. The synergistic CDT and immune therapy effectively improve the anti-tumor efficacy of DDP *in vitro* and *in vivo*. This study demonstrates that TME responsive ROS scavenger/generator shows the potential to reduce side effects of DDP while improve its therapeutic efficacy, providing a new avenue to achieve efficient chemotherapy and promoting the progress of clinical chemotherapy.

1. Introduction

As a widely used chemotherapy drug in clinical, cisplatin (DDP) has been proved to suppress the growth of solid tumor, including lung, ovarian, neck, and bladder cancer. However, its clinical application is impeded by nephrotoxicity [1,2]. About 30 % tumor patients received DDP treatments experience acute kidney injury (AKI) [3]. Although dosage reduction and dose discontinuation have been applied to relieve AKI during clinical DDP treatment, the suppression effect of DDP on solid tumor is reduced as well. AKI has been discovered to be accompanied by the overproduction of reactive oxygen species (ROS), which react with DNA, lipids, and proteins and induce the renal cell injury and dysfunction [4,5]. Antioxidant have been confirmed to reduce the DDP induced AKI via eliminate ROS and maintain normal oxidative stress [6,7]. Among all antioxidant, nanozyme, including copper based nanozyme [8,9], ceria based nanozyme [10,11], and iron based nanozyme [12], with high catalytic activity have attracted much attention to alleviate AKI. Nevertheless, the traditional nanozyme simultaneously eliminates ROS in both kidney and tumor, which is adverse to the anti-tumor effect of chemotherapy agent and hardly fulfills clinical demand. Recently, some tumor microenvironment (TME) responsive nanozyme, that loses its ROS scavenging capacity in tumor, has been developed to alleviate DDP induced AKI without interference with its therapeutic efficacy [13,14]. Unfortunately, this intelligent nanozyme is powerless to improve

* Corresponding author.
** Corresponding author.
*** Corresponding author.
E-mail addresses: fccchengjl@zzu.edu.cn (J. Cheng), roddirck@cqmu.edu.cn (Z. Zhao), baoguojianfeng@gmail.com (J. Bao).
[1] These authors contribute equally to this work.

https://doi.org/10.1016/j.mtbio.2024.101328
Received 5 September 2024; Received in revised form 25 October 2024; Accepted 5 November 2024
Available online 6 November 2024

the efficacy of chemotherapy agent. ROS based therapy, including photodynamic therapy (PDT) [15], chemodynamic therapy (CDT) [16], and sonodynamic therapy (SDT) [17], has been considered as effective strategy to damage tumor cells and suppress the growth of solid tumor. Thus, it is urgent need to develop new nanozyme to decrease ROS level in kidney while increase ROS level in tumor during DDP treatment [18].

Since manganese ion is vital cofactor of numerous metabolic enzymes in human cells, manganese based nanomaterials attracted wide interest in biomedical application [19,20]. Among all manganese based nanomaterials, Mn_3O_4 nanoparticles exhibit multiple antioxidant enzymes activities and act as ROS scavenger to effectively eliminate hydroxyl radical (•OH), singlet oxygen ($^1O_2$), and anion ($O_2^{\cdot-}$) [21,22]. These unique features endow Mn_3O_4 nanoparticles with the capacity to ameliorate inflammation disease, such as ear inflammation and Parkinson's disease [23–25]. Simultaneously, Mn_3O_4 have been proved to degrade in tumor microenvironment with high GSH level and release divalent Mn ions (Mn^{2+}). The released Mn^{2+} could generate ·OH through Fenton-like reaction in tumor, ensuring it with ROS level increasing capacity to realize chemodynamic therapy and overcome insufficient efficacy and resistance of chemotherapy agent [26–31]. These unique features endow Mn_3O_4 nanoparticles as potential switchable ROS generator/scavenger to achieve differentiated management of ROS level in tumor and kidney, which may alleviate the DDP-induced AKI. Moreover, Mn^{2+} has been reported to be a potent agonist to activate the cyclic GMP-AMP synthase stimulator of interferon gene (cGAS-STING) pathway and send an "eat me" signal to the immune system, resulting in the activation of T cell and enhancement of antigen-presenting cells maturation [32–34]. The activated immune response ensure Mn_3O_4 nanoparticles as adjuvant to inhibit the tumor metastases during DDP treatment.

Herein, we develop ultrasmall Mn_3O_4 nanozyme (UMON), that acts as ROS scavenger in kidney while ROS generator in tumor, to alleviate DDP induced AKI and improve the therapeutic efficacy of DDP (Fig. 1). Based on the superoxide dismutase and catalase activity, UMON successfully restores abnormal ROS levels induced by DDP to normal level in kidney and prevent the AKI during DDP treatment *in vitro* and *in vivo*. Once entering the tumor site, UMON switches from ROS scavenger to ROS generator via GSH responsive Mn^{2+} release. The released Mn^{2+} not only works as chemodynamic therapy agent to generate toxic •OH to damage tumor cells, but also successfully initiates the immune response through activating cGAS-STING pathway. The synergistic chemodynamic/immune therapy significantly improve the therapeutic efficacy of DDP and effectively inhibit the metastases of tumor.

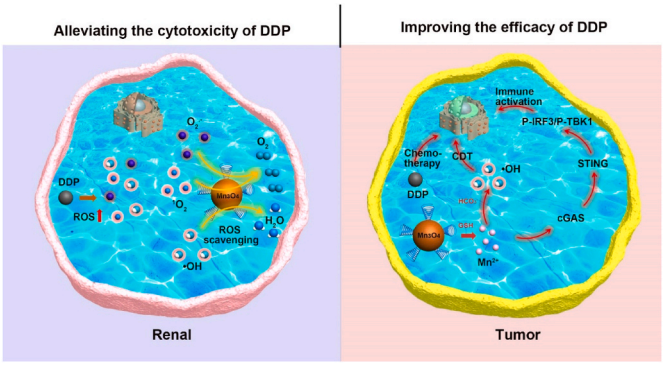

Fig. 1. Schematic cartoon to illustrate the UMON works as ROS scavenger to eliminate ROS while ROS generator and cGAS-STING agonist to improve the therapeutic efficacy of DDP.

2. Results and discussion

2.1. Synthesis and characterization of Mn_3O_4 nanozyme (UMON)

We synthesized the UMON according the published procedure [35]. The transmission electron microscopy (TEM) image indicate that the as-prepare UMON is spherical morphology with uniform size (Fig. 2a). The diameter of UMON is approximately 4.0 nm, which is beneficial to accumulate in kidney. The crystal structure of UMON was investigated by the X-ray diffraction (XRD) and X-ray photoelectron spectroscopy (XPS). The XRD pattern of UMON shows characteristic diffraction peaks, which matches with the typical Mn_3O_4 diffractogram (JCPDS no. 00-24-0734) and demonstrates the as-prepared UMON are Mn_3O_4 (Fig. 2b). Consistent with the XRD analyses, XPS spectra shows that the Mn $2p_{3/2}$ and $2p_{1/2}$ peaks located at 640.4 and 652.1 eV (Fig. 2c). Based on the valence state analyses, we noticed the existence of Mn^{3+}/Mn^{2+} redox couple in UMON with the ratio of 1.6: 1, ensuring UMON with reducibility to restore the reactive oxygen species (ROS) level increase caused by DDP. Subsequently, we analyzed the magnetic property of UMON by a superconducting quantum interference device (SQUID) at room temperature. The field-dependent magnetization ($M-H$) curve of UMON shows straight smooth line without any remanences and coercivities, suggesting that UMON reveals paramagnetic behavior at room temperature (Fig. 2d). We further transfer the as-prepared UMON into aqueous medium by 1,2-distearoyl-sn-glycero-3-phosphoethanolamine-N-[amino(polyethylene glycol)-2000]. The transferred UMON shows excellent colloidal stability in aqueous media. We did not observed any aggregation of transferred UMON after 1 month storage. Dynamic light scattering (DLS) measurements indicate that the hydrodynamic diameter of transferred UMON is slightly larger than its crystal size owing to the existence of hydration layer on the surface of transferred UMON (Fig. S1) [36]. Besides, we investigated the hydrodynamic diameter of UMON in complete medium for 0, 24, and 48 h. It appears that UMON shows good dispersion in physiological environment, which is beneficial for biomedical application (Fig. S2). The zeta potential of transferred UMON is about +9.5 mV (Fig. S3).

2.2. ROS scavenging of UMON in physiological environment

To evaluate the ROS scavenging capacity of UMON, we detected the activity of UMON to eliminate superoxide anion ($O_2^{\cdot-}$), hydroxyl radical (·OH), and singlet oxygen ($^1O_2$) in simulated physiological environment (Fig. 2e). The $O_2^{\cdot-}$ scavenging of UMON was verified by adding UMON into the irradiated solution containing methionine and riboflavin. The nitrotetrazolium blue chloride (NBT) was chose as probe. We observed that the color of NBT and UMON mixture changed from blackish green to brown with the increase of UMON concentration (Fig. 2f). Since the color of UMON is brown, these results suggest that UMON could eliminate $O_2^{\cdot-}$ in concentration dependent manner. The eliminate ratio reaches to 52.8 % when the concentration of UMON is as low as 37.5 μg/mL, indicating the high $O_2^{\cdot-}$ scavenging activity (Fig. 2g). The ·OH scavenging of UMON was investigated by adding UMON into Fe^{2+}/H_2O_2 system using methylene blue (MB) as specific probe. We observed that the absorbance of MB obviously increase in the present of UMON. While there was negligible change of MB could be detected in the absent of UMON (Fig. 2h). Interestingly, the absorption peaks of MB increase with the increase of UMON concentration, resulting in the color of corresponding solution change from colorless to characteristic blue (Fig. S4). It should note that the absorption peak of MB in the solution with 50 mg/mL UMON and ·OH is similar to the MB in the solution without ·OH, indicating the completely ·OH scavenging and demonstrating the strong ·OH scavenging activity of UMON. Subsequently, we investigated the $^1O_2$ scavenging of UMON by electron spin resonance (ESR) spectra using 2,2,6,6-tetramethylpiperidin-1-oxygen (TEMP) as spin trap. It appears that the characteristic peaks of TEMP/$^1O_2$ could be significantly reduced by introducing UMON,

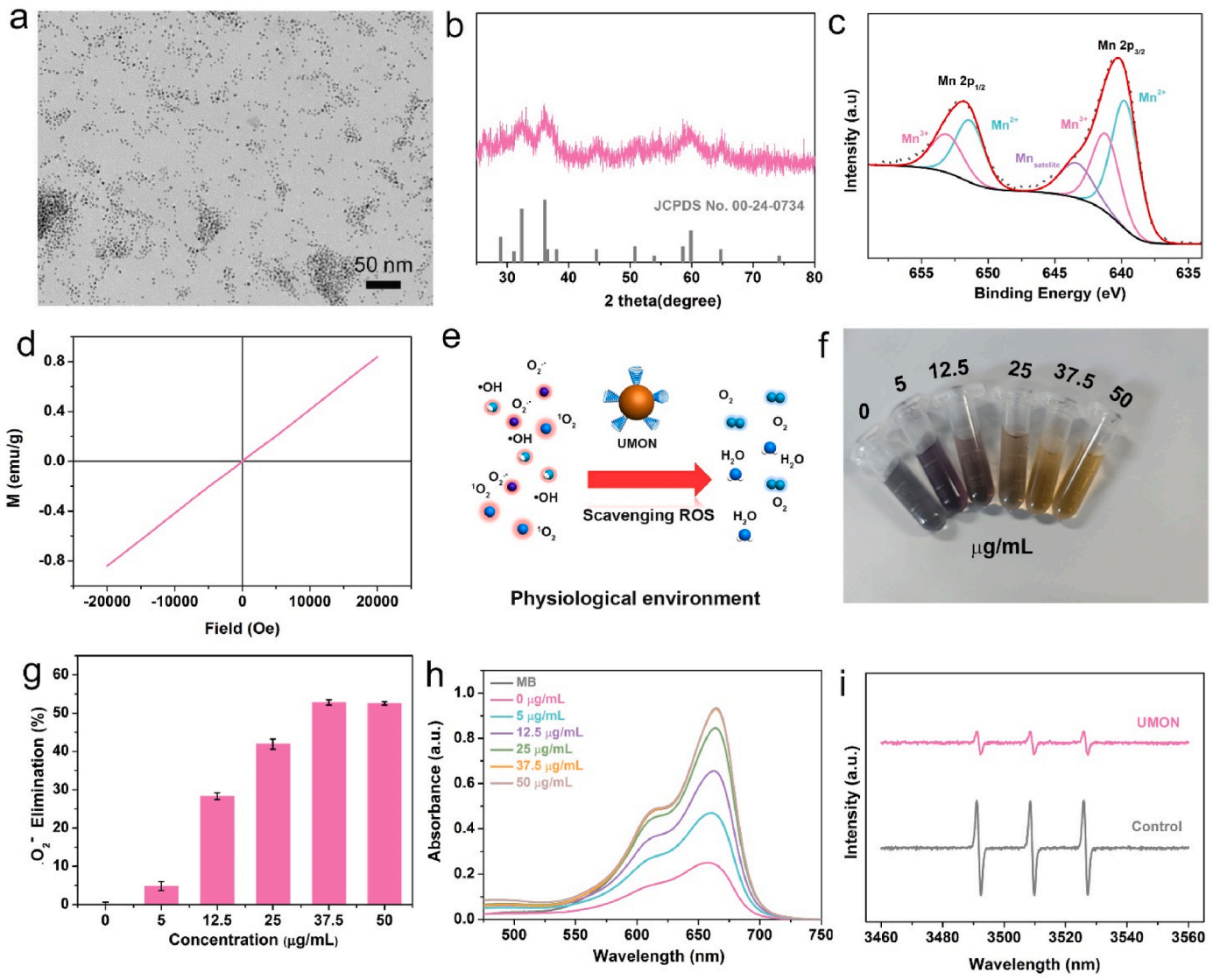

Fig. 2. Characterization of UMON. (a) TEM image of UMON, scale bar is 50 nm. (b) XRD diffraction pattern of UMON. (c) XPS spectrum of UMON in 2p. (d) The smooth *M-H* curve of UMON measured at 300 K using a superconducting quantum interference device magnetometer. (e) The schematic cartoon to illustrate the ROS scavenging of UMON. (f) Digital image that indicates the O_2^- elimination by MPP with different concentration. (g) O_2^- elimination by MPP with different concentration. (h) UV–Vis spectra of MB in the solutions containing ·OH and different concentration of UMON. (i) EPR spectra analyses of $^1O_2$ level in the solution with or without UMON using TEMP as the spin trap.

demonstrating the effective $^1O_2$ scavenging capacity of UMON (Fig. 2i). The above results strongly demonstrate the superior ROS scavenging capacity of UMON in physiological environment, endow it to be potential candidate to alleviate DDP induced AKI [37,38].

2.3. ROS generation in mimic tumor environment

Mn_3O_4 has been reported to degrade into Mn^{2+} in tumor with high GSH level, resulting in the ·OH generation with GSH depletion (Fig. 3a) [39]. This unique feature may endow UMON to switch from ROS scavenger in normal tissue to ROS generator in tumor. The UV–Vis analyses were performed to detect the GSH level with or without UMON using 5, 5′-Dithiobis-(2-nitrobenzoic acid) (DTNB) as probe. We observed obvious decrease in the absorption peak of DTNB after introducing UMON, while negligible change could be noticed without adding UMON (Fig. 3b and Fig. S5). It should note that the degree of decrease in absorption peak of DTNB increases with rising of UMON concentration. The depletion ratio reaches to 62.8 % when the concentration of UMON is as low as 100 μg/mL, revealing the high GSH depletion efficiency and suggesting UMON could sensitively respond to GSH (Fig. 3c). Subsequently, we monitored the Mn^{2+} release kinetics of UMON in the presence of GSH. It appears that GSH significantly accelerates the release of Mn^{2+}, proving the GSH responsive Mn^{2+} release (Fig. 3d). Notably, the release rate was further accelerated by the mild acidic environment. The Mn^{2+} release ratio reaches to 72.3 % in the media with 1 mM GSH and pH 6.5, which is the similar to tumor microenvironment. It should note that the release profile rapidly reaches the plateau, suggesting the quick response of UMON to mimic tumor microenvironment. Based on the successful Mn^{2+} release, we evaluated the feasibility of UMON to generate ·OH using MB as probe. We noted an obvious decrease in the absorbance in the presence of UMON and GSH. Consistent with the Mn^{2+} release profile, we observed the highest ·OH generation efficacy in the mimic tumor microenvironment among all treatment. The degree of decrease in absorption peak of MB increases with rising of UMON concentration (Fig. 3e and Fig. S6). These results strongly prove that UMON successfully switches to ROS generator in TME. The effective generation of ·OH in mimic TME ensure UMON to realize efficient chemodynamic therapy and improve the therapeutic efficacy of DDP. Interestingly, we

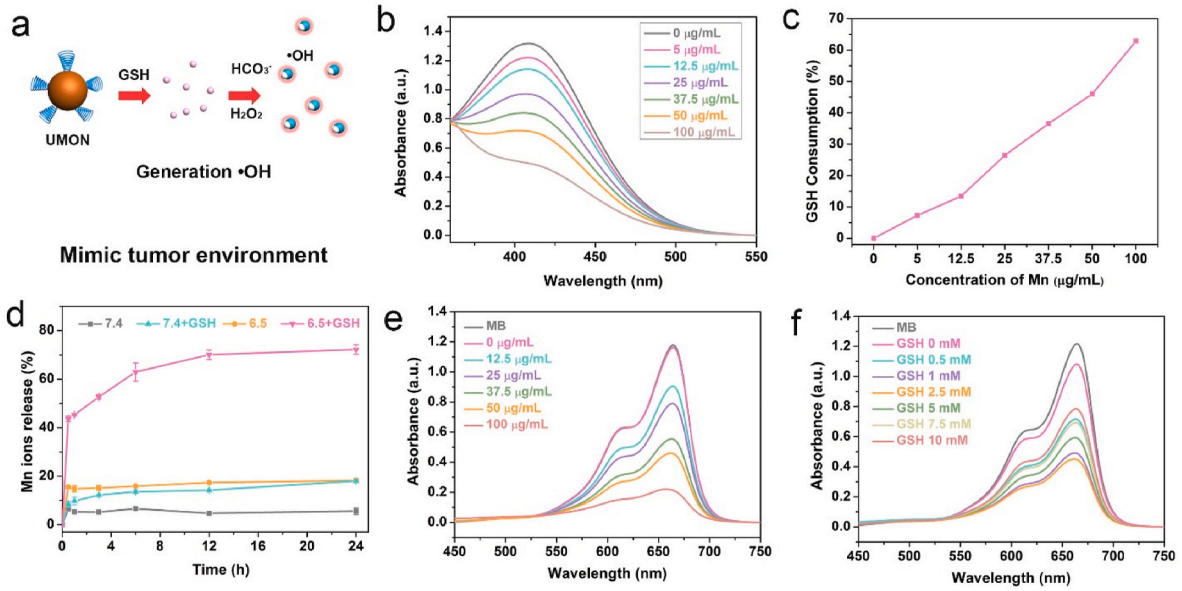

Fig. 3. UMON acts as ROS generator in mimic tumor environment. (a) The schematic cartoon to illustrate that UMON releases Mn^{2+} in TME and generate ·OH. (b) UV–Vis spectra of DTNB in the solutions containing GSH and different concentration of UMON. (c) Depletion ratio of GSH in the solution containing UMON with different concentrations. (d) The Mn^{2+} release profiles of UMON with different treatments. (e) UV–Vis spectra of MB in solution containing different concentration of UMON. (f) UV–Vis spectra MB in solution containing UMON and different concentrations of GSH.

noted that the ·OH generation efficiency rise with the increase of GSH concentration from 0 to 1 mM while decrease with further concentration rising (Fig. 3f and Fig. S7). These phenomena are ascribed to that when GSH is excess along with the increase of GSH concentration, the excessive GSH eliminate the ·OH generated by UMON, resulting in the decrease of ·OH generation efficiency.

2.4. Protective effect on normal renal cells

Since renal tubules are the main target of DDP induced nephrotoxicity [3], we chose human renal tubular epithelial (HK-2) cells as model to investigate the protective effect of UMON on normal renal cells. We analyzed the cytotoxicity of DDP with or without UMON to HK-2 cells by cell-counting-kit-8 (CCK-8) assay. It appears that UMON remarkably increases the viability of HK-2 cells treated by DDP, clearly indicating the protective effect of UMON on normal renal cells (Fig. 4a). It should

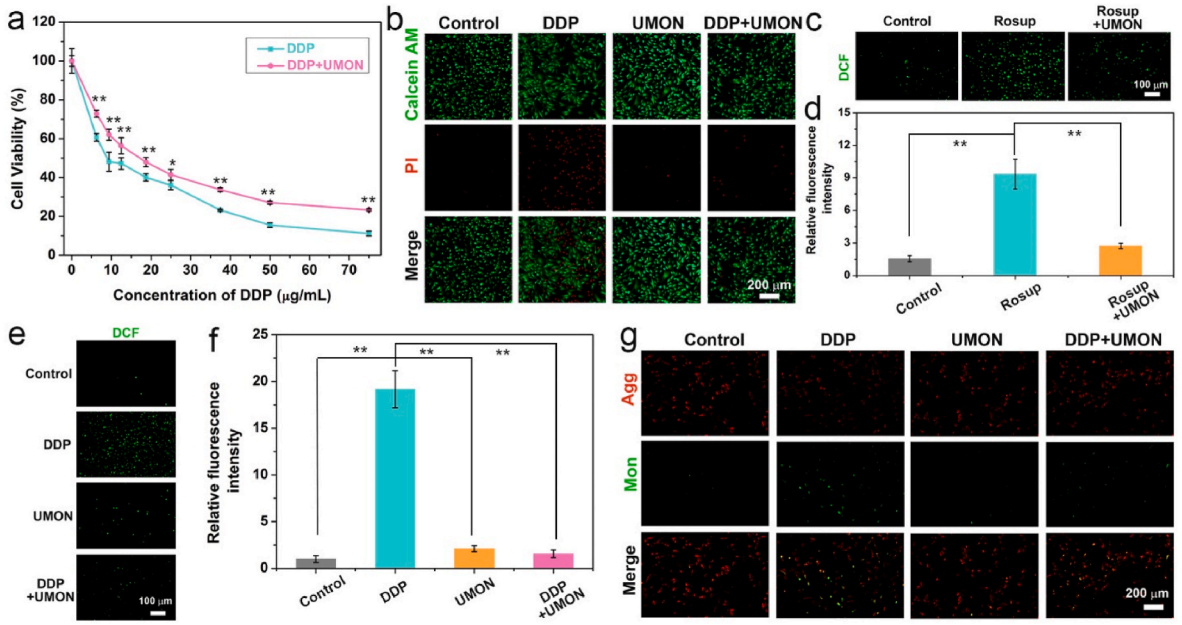

Fig. 4. Protective effect of UMON on normal renal cells. (a) The cell viability of HK-2 cells treated with UMON and different concentrations of DDP (**$p < 0.01$, $n = 5$/group) (b) AM/PI double staining of HK-2 cells with different treatment. (c) Fluorescence images of HK-2 cells incubated with DCFH-DA and PBS, Rosup, and Rosup + UMON. (d) Quantitative fluorescence intensity analyses of HK-2 cells with DCFH-DA and PBS, Rosup, and Rosup + UMON (**$p < 0.01$, $n = 3$/group). (e) Fluorescence images of HK-2 cells incubated with DCFH-DA and PBS, DDP, UMON, and DDP + UMON. (f) Quantitative fluorescence intensity analyses of HK-2 cells with DCFH-DA and PBS, DDP, UMON, and DDP + UMON (**$p < 0.01$, $n = 3$/group). (g) Fluorescence images of HK-2 cells incubated with JC-1 and PBS, DDP, UMON, and DDP + UMON.

mention that there is negligible effect of UMON on the viability of HK-2 cells (Fig. S8). To further verify the protective effect, we stained the HK-2 cells by calcein acetoxymethyl ester (calcein-AM) and propidium iodide (PI). We noted that DDP treated cells showed strong red fluorescence, indicating a larger amount HK-2 cell death and obviously revealing the nephrotoxicity of DDP (Fig. 4b). Notably, the UMON treatment dramatically increases the green fluorescence while decreases the red fluorescence. These results demonstrate that UMON successfully alleviates the nephrotoxicity of DDP to normal renal cells. Since nephrotoxicity of DDP was accompanied with the generation of ROS, we investigated ROS scavenging of UMON in HK-2 cells using 2, 7-Dichlorodihydrofluorescein diacetate (DCFH-DA) as probe. Compared to the cells treated by saline, the cells treated by Rosup [40], that is widely used to increase the ROS level in cell, show evident green fluorescence, corresponding to the increased ROS level in HK-2 cells. Interestingly, UMON treatment remarkably reduces the fluorescence intensity while DDP treatment significantly increases the fluorescence intensity (Fig. 4c and Fig. S9). The quantitative fluorescence analyses indicate that the

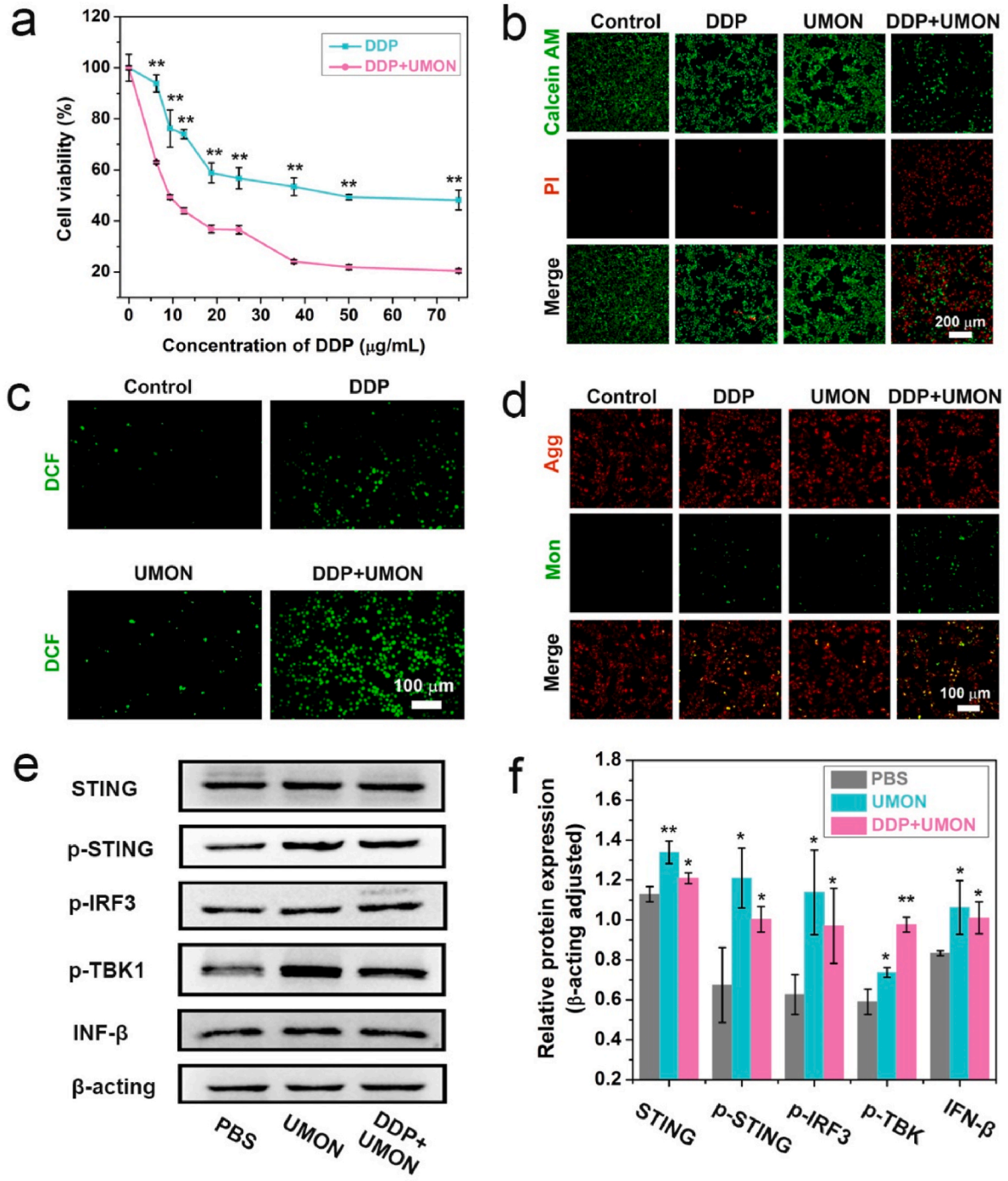

Fig. 5. Improving the efficacy of DDP to tumor cells. (a) The cell viability of 4T1 cells treated with UMON and different concentrations of DDP (**$p < 0.01$, $n = 5$/group). (b) AM/PI double staining of 4T1 cells with different treatment. (c) Fluorescence images of 4T1 cells incubated with DCFH-DA and PBS, DDP, UMON, and DDP + UMON. (d) Fluorescence images of 4T1 cells incubated with JC-1 and PBS, DDP, UMON, and DDP + UMON. (e) Western blot analysis of STING, p-STING, p-IRF3, p-TBK1, and INF-β expression in 4T1 cells with different treatment. (f) Quantitative analysis of STING, p-STING, p-IRF3, p-TBK1, and INF-β expression in in 4T1 cells with different treatment (*$p < 0.05$ and **$p < 0.01$, $n = 3$/group).

relative fluorescence intensity of HK-2 cells treated by Rosup and UMON is about 5.4 times lower than that of HK-2 cells treated by Rosup alone (Fig. 4d). These results strongly support the ROS scavenging activity of UMON in normal renal cells. To visualize the effect of UMON on ROS level of HK-2 cells treated by DDP, we detected the intracellular ROS. Consistent with the nephrotoxicity analyses, we observed strong green fluorescence in the HK-2 cells treated by DDP alone (Fig. 4e). As expected, the UMON treatment significantly decreases the fluorescence intensity owing to its ROS scavenging activity. The quantitative fluorescence analyses indicate that the fluorescence intensity of HK-2 cells treated by DDP and UMON is 1.57, which is 12.2 times lower than that of HK-2 cells treated by DDP alone (Fig. 4f). These results strongly demonstrate that UMON effectively reduce the ROS level and protect normal renal cells during DDP treatment. Since mitochondrial dysfunction caused by abnormal ROS levels is one of the major causes of DDP-induced nephrotoxicity, we measured the mitochondrial function by monitoring mitochondrial membrane potential using 5,5,6,6-tetrachloro-1,1,3,3-tetraethyl-imidacarbocyanine iodide (JC-1) as probe (Fig. 4g). The fluorescence images indicate that the HK-2 cells treated by DDP show the strongest green fluorescence among all treatment, suggest the evidently decrease of mitochondrial membrane potential. Whereas, the HK-2 cells treated by UMON show similar fluorescence to the control group, meaning that UMON successfully maintain the mitochondrial membrane potential at normal level. These results demonstrate that UMON can protect mitochondria from ROS damage caused by DDP in normal renal cells.

2.5. Improving the efficacy of DDP to tumor cells

To verify whether UMON could improve the efficacy of DDP to tumor cells, we chose mouse breast cancer (4T1) cells as model and investigated the effect of UMON on the therapeutic efficacy of DDP. CCK-8 assessment indicates that the 4T1 cells treated by DDP and UMON show lower viability than those treated by DDP alone, suggesting UMON effectively improves the anti-tumor efficacy of DDP. When the concentration of DDP increase to 75 μg/mL, the cell viability treated by both DDP and UMON is about 20.4 %, which is 2.4 times lower than those treated by DDP (Fig. 5a). The improved efficacy could be attributed to the UMON based CDT. We noted that cell viability of 4T1 cells treated by UMON decreased along with the increase of UMON concentration, suggesting that UMON kill tumor cells through CDT (Fig. S10). The improved efficacy of DDP was further supported by the AM/PI co-staining analyses (Fig. 5b). The fluorescence images illustrate that 4T1 cells treated by UMON and DDP show significantly stronger red fluorescence while weaker green fluorescence than those treated by DDP. These results demonstrate that introducing of UMON in the increase of 4T1cell death and suggest the increased tumor killing efficacy of DDP on the assistant of UMON. To investigate whether UMON improve the efficacy of DDP through increase the oxidative stress in 4T1 cells, we visualize the ROS level of 4T1 cells with different treatment (Fig. 5c and Fig. S11). It appears that the fluorescence intensity of cell treated by DDP and UMON are remarkably stronger than that treated by DDP, directly demonstrating that UMON effectively increases the oxidative stress of tumor cells and achieve CDT during DDP treatment. Subsequently, we monitored the mitochondrial membrane potential changes in 4T1 tumor cells by JC-1 to assess the mitochondrial dysfunction (Fig. 5d). Consistent with previous results, the 4T1 cells treated by DDP and UMON show the stronger green fluorescence than those treated by DDP alone. These results suggest that UMON improve the reduction effect of DDP on the mitochondrial membrane potential and increasing effect of DDP on inducing tumor cells to undergo early apoptosis. Activation of the cGAS-STING pathway shows great potential to initiate antitumor immunity. Recently, Mn^{2+} has been discovered as an agonist to effectively activates the cGAS-STING pathway [41,42]. Thus, we further assessed the expression of key protein in the cGAS-STING pathway by Western blot (WB) analyses (Fig. 5e and Fig. S12). It appears that UMON treatment obviously upregulated the expression of STING. The activated STING results in the upregulating of phosphorylated TANK binding kinase 1 (p-TPK1), phosphorylated IRF3 (p-IRF3), phosphorylated STING (p-STING), and interferon-beta (IFN-β). These results demonstrate that UMON could activate the cGAS-STING pathway and enhance the production of inflammatory mediators (Fig. 5f). In addition, we also observed the increased expression of STING, p-STING, p-IRF3, p-TBK1, and IFN-β in cells treated by DDP and UMON. These results clearly indicate that UMON successfully activate the cGAS-STING pathway during DDP treatment and transform tumor from immunosuppressive to immunostimulatory, endowing DDP treatment with capacity to inhibit the tumor metastases.

2.6. Alleviating DDP-induced AKI in vivo

Before investigating the capacity of UMON to alleviate AKI and treat tumor, we assessed its biocompatibility by hemolysis analyses. It appears that the hemolysis rete of red blood cell (RBC) maintained at the safety range after UMON treatment (Fig. S13). The hemolysis rate of RBC treated by 400 μg/mL UMON is about 0.78 %, which is significantly lower than 5 %. Additionally, we assessed the *in vivo* toxicity by analyzing the liver and renal function through blood index analyses (Fig. S14). The blood indexes, including creatinine (CREA), blood urea nitrogen (BUN), aspartate aminotransferase (AST), alanine aminotransferase (ALT), alkaline phosphatase (ALP), and uric acid (UA), are within the normal levels. The H&E staining images also confirm the negligible effect of UMON on the structure of main organs (Fig. S15). These results demonstrate the high biocompatibility of UMON, meaning UMON is suitable to be used as an adjuvant of DDP to alleviate DDP induced AKI.

To verify UMON could alleviate DDP induced AKI, we explored the effect of UMON on AKI mice model established by intraperitoneal injection of DDP. We noted obviously weight loss in saline treated AKI mice compare to healthy mice (Fig. 6a). Whereas, UMON treatment lead to the increase of AKI mice weight, which is close to that of healthy mice. Subsequently, we measured the levels of BUN and CREA, those are clinical renal excretion indicators, in the mice with different treatment to evaluate the therapeutic effect of UMON on AKI mice (Fig. 6b and c). The AKI mice treated by saline show significantly higher BUN and CREA level than healthy mice owing to the abnormal renal function. Interestingly, UMON treatment lead to the reduction of BUN and CREA levels to normal level, suggesting that UMON treatment can effectively restore kidney function. Additionally, we noted that the color of AKI mice kidney treated by UMON is similar to that of healthy mice, which is remarkably darker than AKI mice treated by saline (Fig. 6d). These results strongly supported that UMON successfully relieve the renal injury *in vivo*. To verify the capacity of UMON to alleviate AKI is correlated with its ROS scavenging activity, we visualized the ROS level in the renal tissue using dihydroethidium (DHE) as staining agent (Fig. 6e). The renal tissue of AKI mice treated by saline show dramatically higher DHE signal than healthy mice, which is consistent with the fact that DDP induced AKI is accompanied by the high ROS level. As expected, UMON treatment significantly reduces the increased ROS level caused by the DDP. Besides, we analyzed the expression of kidney injury molecule-1 (KIM-1), which is the typical biomarker of kidney injury (Fig. 6f). It appears that the KIM-1 level of AKI mice treated by UMON is approximately 10.6 pg/mg, which is similar to that of healthy mice while obviously lower than that of AKI mice treated by saline. These results indicate that UMON effectively alleviate kidney injury through reducing ROS level. Furthermore, we assessed the antioxidant activity of renal tissue after different treatment by detecting the level of superoxide dismutase (SOD) and malondialdehyde (MDA). As shown in Fig. 6, the AKI mice treated by UMON show significantly higher SOD level while obviously lower MDA level than AKI mice treated by saline. It should note that the SOD and MDA levels of AKI mice treated by UMON are similar to those of healthy mice, suggesting that UMON restore the

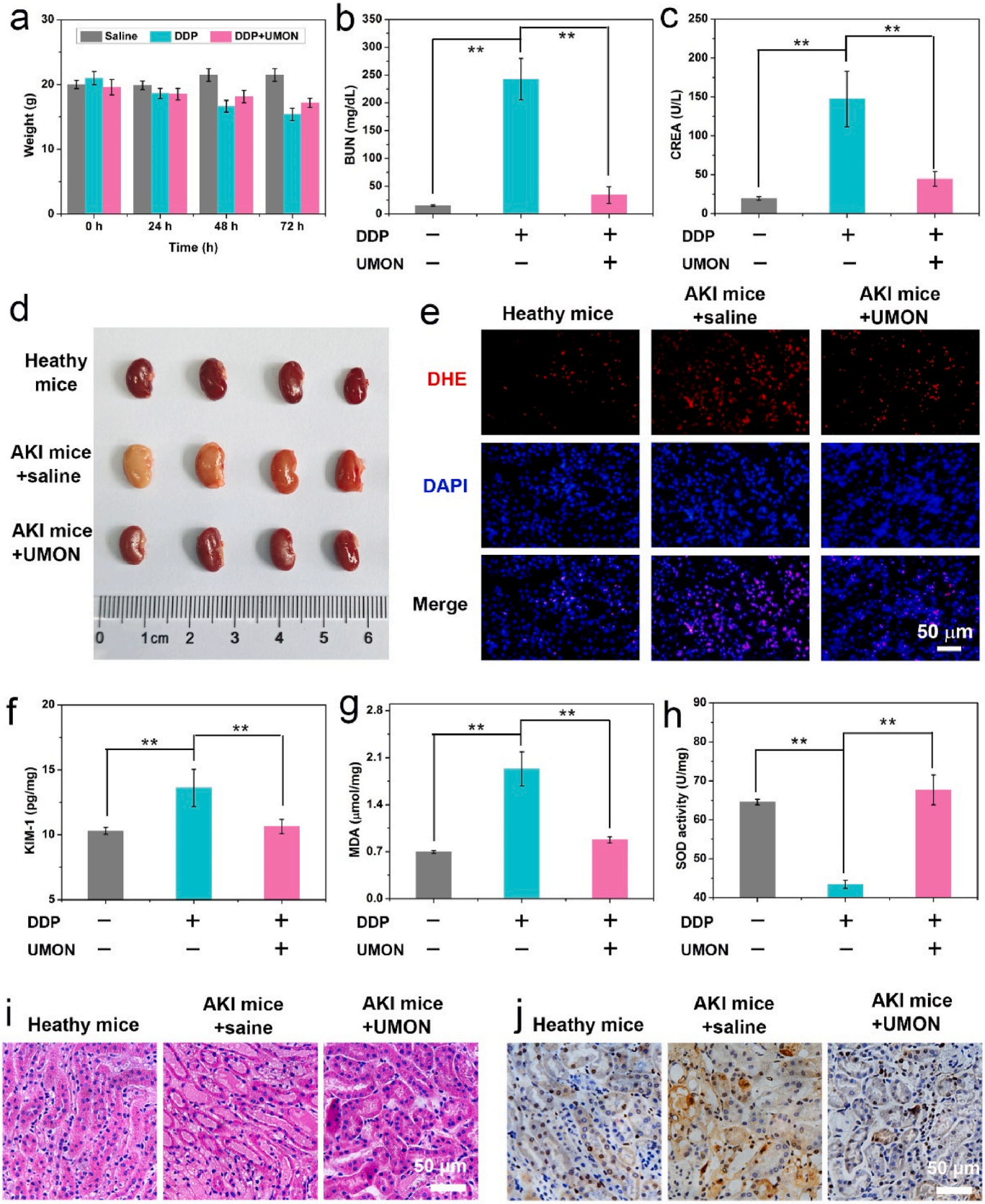

Fig. 6. Alleviating DDP induced AKI in vivo. (a) Body weights of mice with different treatments at 0, 24, 48, and 72 h. (b) BUN and (c) CREA levels in serum of mice with different treatment (**p<0.01, n=4/group). (d) Digital photos of kidney after different treatment. (e) Fluorescence images of renal tissues stained by DHE and DAPI after different treatment. (f) KIM-1 and (g) MDA levels in renal tissue with different treatment (**$p < 0.01$, $n = 4$/group). (h) SOD activity in in renal tissue with different treatment (**$p < 0.01$, $n = 4$/group). (i) H&E and (j) TUNEL staining images of renal tissues with different treatment.

oxidative stress in the kidney of AKI mice (Fig. 6g and h). The alleviation effect of UMON on AKI was further proved by the histopathological analyses. The renal tissue of AKI mice treated by saline show numerous casts, necrotic tubules, and dilated, indicating severe renal injury. Interestingly, the UMON treatment make the renal structure restore to the normal state. No apparent abnormal structure could be observed in the renal tissue of AKI mice treated by UMON (Fig. 6i). Besides, the TUNEL staining images show evident apoptosis signal in AKI mice treated by saline. However, the apoptosis ratio is dramatically reduced with UMON treatment (Fig. 6j). These results show the superior alleviation effect of UMON against DDP induced AKI and endow it as potential candidate to act as an adjuvant of DDP to treat cancer with low side effect.

2.7. Improve efficacy of DDP in vivo

To investigate the improvement effect of UMON on DDP efficacy, we evaluated the therapeutic efficacy of DDP with or without UMON. The 4T1 tumor bearing mice were randomly divided into four groups, those are mice treated by Saline, DDP, UMON, DDP + UMON. The tumor growth curves indicate that the tumors are partially suppressed by the DDP and UMON owing to the DDP based chemotherapy and UMON based CDT (Fig. 7a–d). Notably, the inhibition rate in the mice treated by DDP + UMON is significantly higher compare to the mice treated by DDP. The inhibition rates in the DDP, UMON, and DDP + UMON groups are 39.6 %, 45.8 %, and 62.1 %, respectively. Additionally, the weights and digital photographs show that the sizes and weights of residual tumors in the mice treated by DDP + UMON are obviously reduced compare to the mice treated by DDP alone (Fig. 7e, f and Fig. S16). Subsequently, the therapeutic efficacy was assessed by H&E and TUNEL

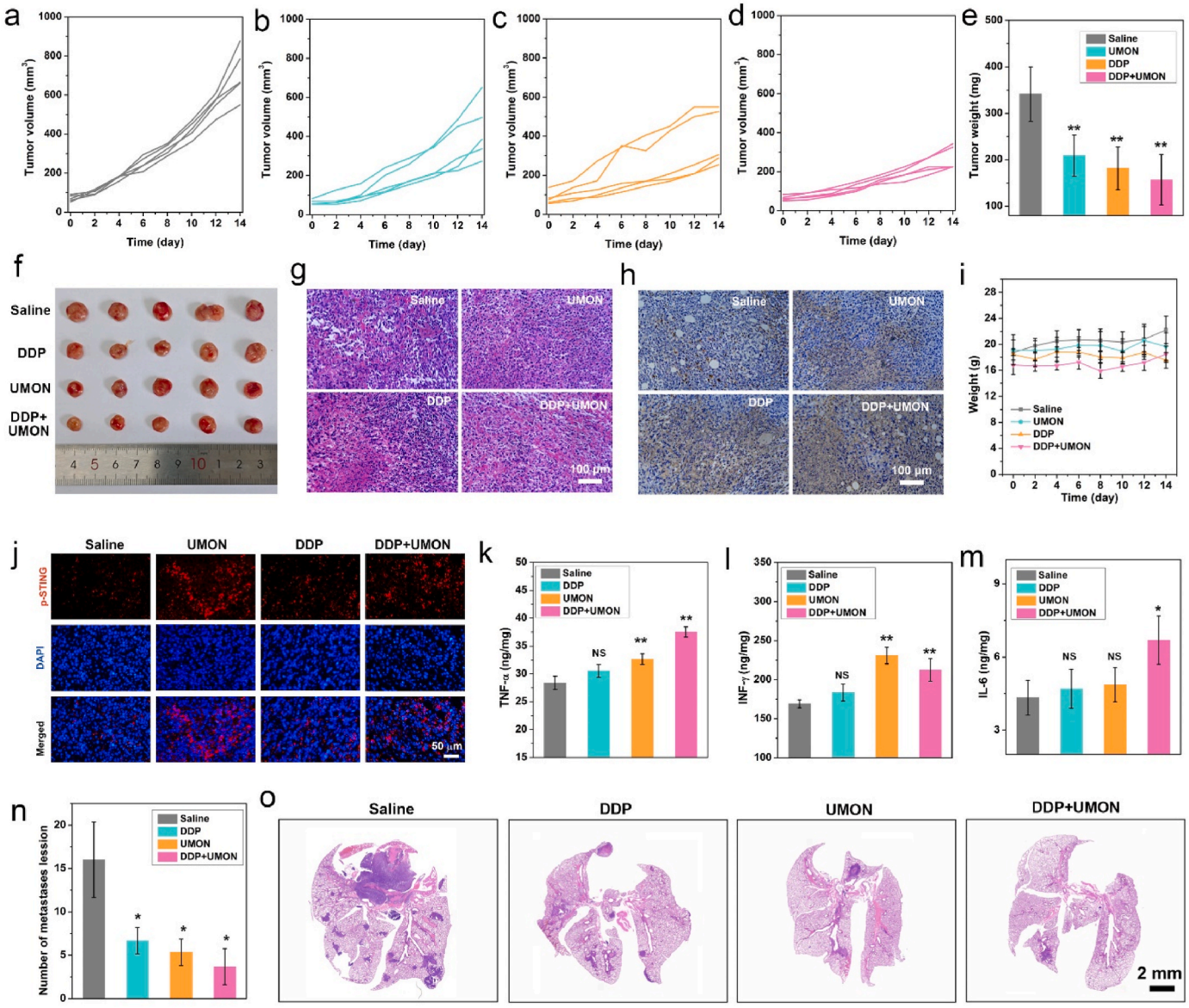

Fig. 7. Improving the therapeutic efficacy of DDP in vivo. Tumor growth curves of tumor bearing mice treated by (a) Saline, (b) DDP, (c) UMON, and (d) DDP + UMON. (e) Tumor weights of mice with different treatments (**$p < 0.01$, $n = 5$/group). (f) Digital photos of tumors after different treatments. (g) H&E and (h) TUNEL staining images of tumor tissues collected from tumor bearing mice with different treatments. (i) Body weights changes of mice with different treatments during treatment. (j) p-STING immunofluorescence images of tumor collected from mice with different treatments. (k) TNF-α, (l) INF-γ, and (m) IL-6 levels in tumor tissues of mice with different treatments (*$p < 0.05$ and **$p < 0.01$, $n = 5$/group). (n) Statistics on the metastases nodules number in the lungs of mice with different treatments (**$p < 0.01$, $n = 5$/group). (o) H&E staining of lung metastases of mice with different treatments.

staining after therapy. The H&E staining images indicate that the tumor of mice treated by DDP + UMON shows more obvious nuclear pyknosis and necrosis than the tumor of mimce treated by DDP and UMON (Fig. 7g). Consistent with the H&E staining analyses, the TUNEL staining image of DDP + UMON shows the strongest green fluorescence in all groups, demonstrating the highest apoptosis level (Fig. 7h). These results suggeste that UMON successfully improves the antitumor effcicay of DDP. It should note that we observe no apparent weights change during the treatment, implying the high biosafety UMON *in vivo* (Fig. 7i). To verify the activation of cGAS-STING pathway by UMON *in vivo*, we detected the p-STING expression by immunofluorescence. It appears that the tumor treated by UMON show evident red fluorescence, which is obviously stronger than tumor treated by DDP and saline (Fig. 7j). These results demonstrate that UMON successfully increase the expression of p-STING and activate the cGAS-STING pathway. Subsequently, we measured the levels of interferon-γ (INF- γ), tumor necrosis factor-α (TNF- α), and interleukin-6 (IL-6) to investigate the immune response of mice treated by UMON (Fig. 7k–m). As expected, the levels of INF- γ, TNF- α, and IL-6 in the mice treated by UMON are remarkably higher than those in the mice treated by saline and DDP. These results indicated that the UMON successfully initiated the antitumor immunity through activating cGAS-STING pathway and motivate us to verify whether UMON could work as an adjuvant to improve efficacy of DDP through inhibiting tumor metastases. We observed apparent metastatic tumor nodules in lung of mice treated by DDP (Fig. S17). The UMON treatment significantly reduce both number and size of metastatic tumor nodules after DDP treatment. The numbers of metastases nodules were about 16, 7, 6, and 3 in mice treated by saline, DDP, UMON, and DDP + UMON, respectively (Fig. 7n). Further H&E staining analyses reveal that there is fewer nuclei enlargement and deep staining in the mice treated by UMON than mice treated by DDP alone (Fig. 7o and Fig. S18). These results demonstrate that UMON effectively inhibit the tumor metastases and work as potential adjuvant to improve efficacy of DDP.

3. Conclusion

In summary, we report ultrasmall Mn_3O_4 nanozyme (UMON) with switchable ROS scavenger and generator activity to alleviate DDP induced AKI with improved the anti-tumor efficacy. In physiological environment, the ROS scavenging activity endow UMON to effectively eliminate excess ROS, restoring abnormal ROS levels caused by DDP in normal renal cells and kidney and alleviating the DDP induced AKI during treatment. Moreover, UMON rapidly respond to high GSH level in tumor and release Mn^{2+}. This unique feature ensures UMON to improve the efficacy of DDP and inhibit the tumor metastases via chemodynamic therapy and successful initiated the immune response through activating cGAS-STING pathway. This intelligent adjuvant integrates with high therapeutic efficacy and low side effect reduction provides a new avenue to effective and safety tumor chemotherapy for future clinical applications.

4. Experimental section

4.1. Synthesis of UMON

To synthesize UMON, 340 mg of manganese (II) acetylacetonate, 314 μL of oleic acid, and 1600 μL of olylamine were dissolved in 30 mL of xylene. The solution was heated to 90 °C, after which 2 mL of deionized water was added with vigorous stirring. The mixture was then aged at 90 °C for 1.5 h. After cooling to room temperature, the UMON were collected and stored in 8 mL hexane at 4 °C. Then, UMON was modified with DSPE-PEG-NH_2 to enhance the biocompatibility. Briefly, UMON (200 μL) and 2 mg of DSPE-PEG-NH_2 were dispersed in 240 μL chloroform and sonicated to ensure them well mixed. After chloroform totally removed, 200 μL of deionized water was added and sonicated again to obtain a uniform monodisperse solution of UMON. The concentration of Mn ions in the solution was detected by ICP-OES.

4.2. OH scavenging activity of UMON

$FeSO_4$ (1.8 mM, 350 μL) was mixed with H_2O_2 (5 mM, 350 μL) and incubated at 37 °C for 15 min. Then UMON with final concentrations of 0, 5, 12.5, 25, 37.5, 50 μg/mL and MB (100 μL, 100 μg/mL) were added to the mixed solution and stirred for 1 h. After the reaction was finished, The absorbance of solution at 475–750 nm was measured by the UV–Vis spectroscopy.

4.3. O_2^- scavenging activity of UMON

Methionine (130 mM,150 μL), riboflavin (200 μM, 150 μL), NBT (750 μM,150 μL), and UMON with final concentrations of 0, 5, 12.5, 25, 37.5, 50 μg/mL were added to deionized water and fixed the final volume to 1.5 mL, respectively. Then the mixed solutions were irradiated with a 365 nm UV lamp for 15 min. Following, the absorbance at 560 nm was measured immediately by a microplate reader. The scavenging efficiency was calculated using the formula: elimination rate (%) = $[(A_0\text{-}A)/A_0] \times 100$ %, where A is the absorbance of the sample and A_0 is the absorbance of the control.

4.4. $^1O_2$ scavenging activity of UMON

The scavenging activity of UMON against $^1O_2$ was assessed using electron spin resonance (ESR) spectroscopy. To generate $^1O_2$, hydrogen peroxide (H_2O_2, 7.5 mM, 200 μL) was mixed with sodium hypochlorite (2.5 mM, 200 μL) and incubated for 5 min. Subsequently, UMON (0, 50 μg/mL), TEMP ($^1O_2$ trapping agent), and deionized water we added to a total volume of 1.6 mL and incubated for another 5 min. The residue $^1O_2$ was traped by TEMP and the ESR spectra were recorded by Bruker A300-10/12 sepctrometer.

4.5. OH generation of UMON

The generation of·OH by UMON was evaluated using MB as an indicator. Briefly, glutathione (GSH) at final concentrations of 0, 0.5, 1, 2.5, 5, 7.5, and 10 mM was mixed with UMON at final concentrations of 0, 12.5, 25, 37.5, 50, and 100 μg/mL in PBS (pH 6.5 or 7.4) and incubated at room temperature for 30 min. Then centrifuged and samplied 190 μL of supernatant, H_2O_2 (100 mM, 200 μL), MB (100 μg/mL, 200 μL), and $NaHCO_3$ (25 mM, 1400 μL) were added sequentially and incubate at 37 °C for 45 min. Finally, the absorbance of solution at 450–750 nm was measured by the UV–Vis spectroscopy.

4.6. Cytotoxicity evaluation in HK-2 cells

The HK-2 cells were seeded in 96-well plate at a density of 1×10^4 cells per well for 24 h to allow cell attachment. Subsequently, the medium was removed and the cells were washed with PBS, and then fresh complete medium containing UMON (0, 0.94, 1.88, 3.75, and 7.5 μg/mL) was added. After incubation for 24 h, the cells were washed with PBS, 10 μL of CCK-8 and 100 μL of fresh DMEM/F12 and incubated for 45 min. The absorbance of each well was measured by a microplate reader at 450 nm, and the cell viability was calculated.

4.7. HK-2 cells protection by UMON

The HK-2 cells were seeded in 96-well plate at a density of 1×10^4 cells per well for 24 h to allow cell attachment. Subsequently, the medium was removed and the cells were washed with PBS, and then fresh complete medium containing DDP (0, 6.25, 9.375, 12.5, 18.75, 25, 37.5, 50, 75 μg/mL), UMON (5 μg/mL) + DDP (0, 6.25, 9.375, 12.5, 18.75, 25, 37.5, 50, 75 μg/mL) were added, respectively. After incubation for 24 h, the cells were washed with PBS, and 10 μL of CCK-8 and 100 μL of fresh

DMEM/F12 and incubated for 45 min. The absorbance of each well was measured by a microplate reader at 450 nm, and the cell viability was calculated.

4.8. Calcium fluorescein (AM) and PI staining in HK-2 cells

The HK-2 cells were seeded in 96-well plate and incubated overnight, followed by treated with UMON (5 μg/mL), DDP (5 μg/mL), UMON (5 μg/mL) + DDP (5 μg/mL), respectively. After 12 h, the cells were stained with both Calcein-AM and PI for 15 min. The fluorescence intensities were monitored with a fluorescent microscopy (Leica DM 3000).

4.9. Mitochondrial membrane potential measurement in HK-2 cells

HK-2 cells were seeded in the 96-well plate at a density of 1.5×10^4 cells per well and incubated overnight. Then the medium was extracted and the cells were washed with the PBS, followed by addition of UMON (5 μg/mL), DDP (5 μg/mL), UMON (5 μg/mL) + DDP (5 μg/mL), respectively. After 12 h, the cells were washed with PBS and stained with JC-1 for 30 min. Lastly, cells were washed with buffer solution, and fluorescent microscopy was performed to acquire the fluorescence images.

4.10. ROS scavenging activity in HK-2 cells

HK-2 cells were seeded in the 96-well plate at a density of 1.5×10^4 cells per well. Rosup (50 μg/mL) was dispersed in RPMI 1640 medium and added to the cells for 2 h incubation at 37 °C to produce ROS. Subsequently the supernatants were removed and the cells were incubated with UMON (5 μg/mL), DDP (5 μg/mL), UMON (5 μg/mL) + DDP (5 μg/mL), respectively. After 4 h, we removed the medium again and added DCFH-DA 30 min incubation. The fluorescence of DCF was observed under fluorescence microscopy.

4.11. ROS generation in 4T1 cells

4T1 cells were seeded in the 96-well plate at a density of 1.5×10^4 cells per well and incubated overnight allow for attachment. UMON (15 μg/mL), DDP (10 μg/mL), UMON (15 μg/mL) + DDP (10 μg/mL) were added to the cells and incubated for 8 h, respectively. Following treatment, the cells were incubated with DCFH-DA for 30 min, the generation of ROS was assessed by observing the DCF fluorescence under a fluorescence microscope.

4.12. Stimulation of STING pathway in 4T1 cells

4T1 cells were seeded in the 6-well plate at a density of 2×10^5 cells per well and incubated overnight. Then the medium was extracted and the cells were washed with the PBS, followed by addition of UMON (5 μg/mL), UMON (5 μg/mL) + DDP (10 μg/mL). After 24 h, the cells were split with RIPA lysis buffer for 30 min and centrifugated (12000 g, 5 min) at 4 °C. Then we used the BCA protein kit (Dalian Meilun Biotechnology Co. Ltd.) to measure the protein concentration of the supernatant. The acquired protein was separated by 10 % SDS-PAGE gel electrophoresis and transferred onto PVDF membranes. The PVDF membranes were examined by using Chemiluminescence imaging system (Guangzhou Light Instrument Biotechnology Co. LTD, OI-600) after incubation with primary antibody for 12 h at 4 °C and horseradish peroxidase-labelled secondary antibody. The antibodies used in this study were as follows: STING (Proteintech), p-STING (Proteintech), p-PIRF3 (ABclonal), p-TBK1 (ABclonal), IFN-β(ABclonal), and β-actin (ABclonal).

4.13. AKI model establishment

Animal experiments were conducted according to the protocol approved by the Institutional Animal Care and Use Committee of the First Affiliated Hospital of Zhengzhou University. The cisplatin (DDP)-induced AKI models were established with a dose of 12.5 mg/kg 72 h post-injection, mice were sacrificed to collect blood and renal tissues for kidney function analysis and histological analysis, respectively.

4.14. Assessment of therapeutic effects on AKI mice

To evaluate the therapeutic effects of UMON, mice were randomly divided into 3 groups with different treatments: Saline, DDP, DDP + UMON group. After injected DDP to induced AKI models 2 h, 100 μL saline and UMON with 6 mg/kg concentration of Mn ions was injected into AKI mice via tail vein. 24, 48, 72 h post-injection, the body weight variations in each group ($n = 4$) were monitored. Then all mice were sacrificed, blood samples were used to extract serum for detecting the renal function levels (BUN and CREA). The right kidneys were harvested and cut into two equal sections. One section was stained by DHE to detect ROS levels. The other section was extracted for the detection of KIM-1, malondialdehyde (MDA) and superoxide dismutase (SOD) levels. The left kidneys were fixed with 4 % paraformaldehyde for the hematoxylin and eosin (H&E) and Terminal Deoxynucleotidyl Transferase-Mediated dUTP Nick End Labeling (TUNEL) staining to assess the renal protection effects of UMON.

4.15. Tumor therapy in vivo

4T1 bearing Balb/c mice were randomly divided into 4 groups with different treatments: Saline, UMON, DDP, DDP + UMON group. DDP was intraperitoneally injected at the dosage of 3 mg/kg (once a week), and UMON were intravenously injected at the dosage of 6 mg/kg (once in four days.), respectively. The tumor growth and body weight changes of mice monitored every 2 days until day 14. Then all mice were sacrificed, the tumors were harvested and stained with H&E and TUNEL. For the Stimulation of STING Pathway *in vivo*, we evaluated the levels of p-STING protein expression in the tumor region using immunofluorescence staining.

4.16. Lung metastasis inhibition of UMON

Tumor-bearing Balb/c mice with tumor size of about 75–100 mm were randomly divided into four groups, Saline, UMON, DDP, DDP + UMON group. After the 14-day treatment, the primary tumor was surgically resected and recovered without any treatment for 5 days. These mice were injected with 4×10^5 4T1 cells via tail vein. 18 days post-injection, the mice were sacrificed and the lung tissues were extracted to count the number of surface metastases and to record the number of internal metastases by H&E staining.

Funding

This work was supported by National Natural Science Foundation of China (No. 82271974), The Key Technologies R&D Programme of Henan Province (No. 242102311243), Natural Science Foundation of Henan Province (No. 222300420562), and Heluo Youth Talent Support Project (No.2023HLTJ19).

CRediT authorship contribution statement

Yanan Ren: Writing – original draft, Methodology, Investigation, Formal analysis, Data curation, Conceptualization. **Fei Wu:** Investigation, Formal analysis, Data curation. **Linlin Huo:** Investigation, Formal analysis, Data curation. **Xiao Wang:** Investigation, Formal analysis. **Yong Zhang:** Investigation. **Mengke Fan:** Investigation. **Mingya Tan:** Investigation. **Jiayi Zhao:** Investigation. **Jingliang Cheng:** Methodology, Investigation, Funding acquisition, Conceptualization. **Zhenghuan Zhao:** Writing – review & editing, Formal analysis, Conceptualization.

Jianfeng Bao: Writing – review & editing, Funding acquisition, Formal analysis, Conceptualization.

Declaration of competing interest

The authors declare that they have no known competing financial interests or personal relationships that could have appeared to influence the work reported in this paper.

Appendix A. Supplementary data

Supplementary data to this article can be found online at https://doi.org/10.1016/j.mtbio.2024.101328.

Data availability

Data will be made available on request.

References

[1] C. Zhang, C. Xu, X. Gao, Q. Yao, Platinum-based drugs for cancer therapy and anti-tumor strategies, Theranostics 12 (5) (2022) 2115–2132.
[2] S. Latcha, E.A. Jaimes, S. Patil, I.G. Glezerman, S. Mehta, C.D. Flombaum, Long–term renal outcomes after cisplatin treatment, Clin. J. Am. Soc. Nephrol. 11 (7) (2016).
[3] C. Tang, M.J. Livingston, R. Safirstein, Z. Dong, Cisplatin nephrotoxicity: new insights and therapeutic implications, Nat. Rev. Nephrol. 19 (1) (2023) 53–72.
[4] S. He, C. Chen, F. Li, W. Xu, D. Li, M. Liang, et al., A polymeric nanosponge as a broad-spectrum reactive oxygen species scavenger for acute kidney injury treatment, Nano Lett. 23 (19) (2023) 8978–8987.
[5] X. Zhao, L.-Y. Wang, J.-M. Li, L.-M. Peng, C.-Y. Tang, X.-J. Zha, et al., Redox-mediated artificial non-enzymatic antioxidant MXene nanoplatforms for acute kidney injury alleviation, Adv. Sci. 8 (18) (2021) 2101498.
[6] C-y Fang, D-y Lou, L-q Zhou, J-c Wang, B. Yang, Q-j He, et al., Natural products: potential treatments for cisplatin-induced nephrotoxicity, Acta Pharmacol. Sin. 42 (12) (2021) 1951–1969.
[7] T. Sun, D. Jiang, Z.T. Rosenkrans, E.B. Ehlerding, D. Ni, C. Qi, et al., A melanin-based natural antioxidant defense nanosystem for theranostic application in acute kidney injury, Adv. Funct. Mater. 29 (48) (2019) 1904833.
[8] L. Xu, Z. Xing, J. Yuan, Y. Han, Z. Jiang, M. Han, et al., Ultrasmall nanoparticles regulate immune microenvironment by activating IL-33/ST2 to alleviate renal ischemia-reperfusion injury, Adv. Healthcare Mater. 13 (13) (2024) 2303276.
[9] B. Bao, H. Liu, Y. Han, L. Xu, W. Xing, Z. Li, Simultaneous elimination of reactive oxygen species and activation of nrf2 by ultrasmall nanoparticles to relieve acute kidney injury, ACS Appl. Mater. Interfaces 15 (13) (2023) 16460–16470.
[10] H. Yu, F. Jin, D. Liu, G. Shu, X. Wang, J. Qi, et al., ROS-responsive nano-drug delivery system combining mitochondria-targeting ceria nanoparticles with atorvastatin for acute kidney injury, Theranostics 10 (5) (2020) 2342–2357.
[11] D.-Y. Zhang, H. Liu, C. Li, M.R. Younis, S. Lei, C. Yang, et al., Ceria nanozymes with preferential renal uptake for acute kidney injury alleviation, ACS Appl. Mater. Interfaces 12 (51) (2020) 56830–56838.
[12] Z. Xu, Y. Zhu, M. Xie, K. Liu, L. Cai, H. Wang, et al., Mackinawite nanozymes as reactive oxygen species scavengers for acute kidney injury alleviation, J. Nanobiotechnol. 21 (1) (2023) 281.
[13] Q. Weng, H. Sun, C. Fang, F. Xia, H. Liao, J. Lee, et al., Catalytic activity tunable ceria nanoparticles prevent chemotherapy-induced acute kidney injury without interference with chemotherapeutics, Nat. Commun. 12 (1) (2021) 1436.
[14] X. Gao, B. Wang, J. Li, B. Niu, L. Cao, X-j Liang, et al., Catalytic tunable black phosphorus/ceria nanozyme: a versatile oxidation cycle accelerator for alleviating cisplatin-induced acute kidney injury, Adv. Healthcare Mater. 12 (30) (2023) 2301691.
[15] M. Overchuk, R.A. Weersink, B.C. Wilson, G. Zheng, Photodynamic and photothermal therapies: synergy opportunities for nanomedicine, ACS Nano 17 (9) (2023) 7979–8003.
[16] P. Zhao, H. Li, W. Bu, A forward vision for chemodynamic therapy: issues and opportunities, Angew. Chem. Int. Ed. 62 (7) (2023) e202210415.
[17] S. Li, G.S.P. Mok, Y. Dai, Lipid bilayer-based biological nanoplatforms for sonodynamic cancer therapy, Adv. Drug Deliv. Rev. 202 (2023) 115110.
[18] S. Zhu, L. Huo, J. Zeng, R. Chen, Y. Sun, M. Tan, et al., Differentiated management of ROS level in tumor and kidney to alleviate Cis-platinum induced acute kidney injury with improved efficacy, J. Nanobiotechnol. 22 (1) (2024) 436.
[19] B. Ding, P. Zheng, Pa Ma, J. Lin, Manganese oxide nanomaterials: synthesis, properties, and theranostic applications, Adv. Mater. 32 (10) (2020) 1905823.
[20] M. Tang, Z. Zhang, T. Sun, B. Li, Z. Wu, Manganese-based nanozymes: preparation, catalytic mechanisms, and biomedical applications, Adv. Healthcare Mater. 11 (21) (2022) 2201733.
[21] G. Huang, J. Zang, L. He, H. Zhu, J. Huang, Z. Yuan, et al., Bioactive nanoenzyme reverses oxidative damage and endoplasmic reticulum stress in neurons under ischemic stroke, ACS Nano 16 (1) (2022) 431–452.
[22] M. Liu, H. Wu, Q. Li, H. Liu, C. Chen, F. Yin, et al., Mn3O4 nanozymes prevent acetaminophen-induced acute liver injury by attenuating oxidative stress and countering inflammation, J. Colloid Interface Sci. 654 (2024) 83–95.
[23] J. Yao, Y. Cheng, M. Zhou, S. Zhao, S. Lin, X. Wang, et al., ROS scavenging Mn3O4 nanozymes for in vivo anti-inflammation, Chem. Sci. 9 (11) (2018) 2927–2933.
[24] N. Singh, M.A. Savanur, S. Srivastava, P. D'Silva, G. Mugesh, A redox modulatory Mn3O4 nanozyme with multi-enzyme activity provides efficient cytoprotection to human cells in a Parkinson's disease model, Angew. Chem. Int. Ed. 56 (45) (2017) 14267–14271.
[25] Z. Xu, A. Qu, W. Wang, M. Lu, B. Shi, C. Chen, et al., Facet-dependent biodegradable Mn3O4 nanoparticles for ameliorating Parkinson's disease, Adv. Healthcare Mater. 10 (23) (2021) 2101316.
[26] W. Li, R. Li, Q. Ye, Y. Zou, X. Lu, W. Zhang, et al., Mn3O4 nanoshell coated metal–organic frameworks with microenvironment-driven O2 production and GSH exhaustion ability for enhanced chemodynamic and photodynamic cancer therapies, Adv. Healthcare Mater. 12 (15) (2023) 2202280.
[27] Y. Bian, B. Liu, B. Ding, M. Wang, M. Yuan, Pa Ma, et al., Tumor microenvironment-activated nanocomposite for self-amplifying chemodynamic/starvation therapy enhanced Ido-blockade tumor immunotherapy, Adv. Sci. 10 (34) (2023) 2303580.
[28] C. Qi, J. He, L.-H. Fu, T. He, N.T. Blum, X. Yao, et al., Tumor-specific activatable nanocarriers with gas-generation and signal amplification capabilities for tumor theranostics, ACS Nano 15 (1) (2021) 1627–1639.
[29] L.-H. Fu, Y.-R. Hu, C. Qi, T. He, S. Jiang, C. Jiang, et al., Biodegradable manganese-doped calcium phosphate nanotheranostics for traceable cascade reaction-enhanced anti-tumor therapy, ACS Nano 13 (12) (2019) 13985–13994.
[30] K. Zhang, C. Qi, K. Cai, Manganese-based tumor immunotherapy, Adv. Mater. 35 (19) (2023) 2205409.
[31] L.-H. Fu, Y. Wan, C. Li, C. Qi, T. He, C. Yang, et al., Biodegradable calcium phosphate nanotheranostics with tumor-specific activatable cascade catalytic reactions-augmented photodynamic therapy, Adv. Funct. Mater. 31 (14) (2021) 2009848.
[32] M. Lv, M. Chen, R. Zhang, W. Zhang, C. Wang, Y. Zhang, et al., Manganese is critical for antitumor immune responses via cGAS-STING and improves the efficacy of clinical immunotherapy, Cell Res. 30 (11) (2020) 966–979.
[33] Z. Sun, Z. Wang, T. Wang, J. Wang, H. Zhang, Z. Li, et al., Biodegradable MnO-based nanoparticles with engineering surface for tumor therapy: simultaneous fenton-like ion delivery and immune activation, ACS Nano 16 (8) (2022) 11862–11875.
[34] S.-J. Zheng, M. Yang, J.-Q. Luo, R. Liu, J. Song, Y. Chen, et al., Manganese-based immunostimulatory metal–organic framework activates the cGAS-STING pathway for cancer metalloimmunotherapy, ACS Nano 17 (16) (2023) 15905–15917.
[35] M. Li, L. Huo, J. Zeng, G. Zhu, X. Liu, X. Zhu, et al., Switchable ROS scavenger/generator for MRI-guided anti-inflammation and anti-tumor therapy with enhanced therapeutic efficacy and reduced side effects, Adv. Healthcare Mater. 12 (5) (2023) 2202043.
[36] V.N. Koparde, P.T. Cummings, Molecular dynamics study of water adsorption on TiO2 nanoparticles, J. Phys. Chem. C 111 (19) (2007) 6920–6926.
[37] H. Yuan, F. Wang, Z. Wang, D. Gu, W. Huang, C. Fu, et al., Natural metal polyphenol nanozyme: free radical scavenging and antioxidation for the treatment of acute kidney injury, ACS Mater. Lett. 5 (10) (2023) 2807–2819.
[38] Y. Zheng, H. Yi, Z. Zhan, S.-S. Xue, G. Tang, X. Yu, et al., Reactive oxygen/nitrogen species scavenging and inflammatory regulation by renal-targeted bio-inspired rhodium nanozymes for acute kidney injury theranostics, J. Colloid Interface Sci. 662 (2024) 413–425.
[39] X. Zhu, H. Xiong, P. Yang, S. Wang, Q. Zhou, P. Zhang, et al., A pH/GSH dual responsive nanoparticle with relaxivity amplification for magnetic resonance imaging and suppression of tumors and metastases, Nanoscale 15 (4) (2023) 1583–1594.
[40] S-j Li, B. Cao, Z-y Lu, R-b Sun, S-h Guo, Y. Xie, et al., Cystine supplementation rebalances the redox homeostasis of microenvironment in non-small cell lung cancer cells and reverses their resistance to docetaxel, Acta Pharmacol. Sin. 42 (12) (2021) 2132–2143.
[41] Peng Y, Liang S, Liu D, Ma K, Yun K, Zhou M, et al. Multi-metallic nanosheets reshaping immunosuppressive tumor microenvironment through augmenting cGAS-STING innate activation and adaptive immune responses for cancer immunotherapy. Adv. Sci.n/a(n/a):2403347.
[42] H. Lin, C. Jiang, B. Wang, Y. Wang, Z. Shangguan, Y. Wu, et al., Glutathione degradable manganese-doped polydopamine nanoparticles for photothermal therapy and cGAS-STING activated immunotherapy of lung tumor, J. Colloid Interface Sci. 663 (2024) 167–176.